Supplemental Material: Optical Control of Slow Topological Electrons in Moiré Systems

Christopher Yang, Iliya Esin, Cyprian Lewandowski, and Gil Refael

I. DETAILS OF THE MODELS

In both the toy and continuum models, we take the undriven Hamiltonians $H(\boldsymbol{k})$ and obtain the time-dependent Hamiltonian $H(\boldsymbol{k},t)$ via minimal coupling $\boldsymbol{k} \to \boldsymbol{k} + e\boldsymbol{A}(t)/\hbar$. Here,

$$\boldsymbol{A}(t) = A[\cos(\Omega t)\hat{\boldsymbol{x}} - \sin(\Omega t)\hat{\boldsymbol{y}}] \tag{S1}$$

is the magnetic vector potential of the circularly polarized laser. We can expand the time-dependent eigenstates of the Hamiltonian in a Floquet-Bloch basis [1]:

$$|\psi_{\boldsymbol{k}\alpha}(t)\rangle = e^{-i\varepsilon_\alpha^{(\xi)}t/\hbar}|\Phi^m_{\boldsymbol{k}\alpha}(t)\rangle, \tag{S2}$$

where $|\Phi^m_{\boldsymbol{k}\alpha}(t)\rangle$ is periodic in time ($|\Phi^m_{\boldsymbol{k}\alpha}(t)\rangle = |\Phi^m_{\boldsymbol{k}\alpha}(t + 2\pi/\Omega)\rangle$), $\varepsilon_\alpha^{(\xi)}$ are the quasienergies plotted in Fig. 2(d), and α enumerates the Floquet quasienergy bands. To determine the Floquet-Bloch basis, it is easiest to expand the time-dependent $|\Phi^m_{\boldsymbol{k}\alpha}(t)\rangle$ in terms of time-independent Fourier harmonics $|\phi^m_{\boldsymbol{k}\alpha}\rangle$,

$$|\Phi^m_{\boldsymbol{k}\alpha}(t)\rangle = \sum_m e^{-im\Omega t}|\phi^m_{\boldsymbol{k}\alpha}\rangle, \tag{S3}$$

take a Fourier transform the Hamiltonian,

$$H(\boldsymbol{k},t) = \sum_m e^{-im\Omega t}H^{(m)}(\boldsymbol{k}), \tag{S4}$$

and solve the Schrödinger equation in the basis of Floquet harmonics:

$$(\varepsilon_\alpha^{(\xi)} + m\hbar\Omega)|\phi^m_{\boldsymbol{k}\alpha}\rangle = \sum_{m'} H^{(m-m')}(\boldsymbol{k})|\phi^{m'}_{\boldsymbol{k}\alpha}\rangle. \tag{S5}$$

In the following subsections, we detail the exact form of the Floquet Hamiltonians.

A. Tight binding Floquet toy Hamiltonian

We use a rescaled, two-band tight binding model for graphene to replicate the flat conduction and valence bands of TBG. In the rescaled Hamiltonian

$$H_{\text{toy}}(\boldsymbol{k}) = \begin{pmatrix} 0 & h_{\boldsymbol{k}} \\ h^*_{\boldsymbol{k}} & 0 \end{pmatrix}, \tag{S6}$$

$$h_{\boldsymbol{k}} = \frac{W}{3}\sum_j e^{i\boldsymbol{k}\cdot\boldsymbol{\delta}_j}, \tag{S7}$$

we choose long hopping vectors

$$\boldsymbol{\delta}_j = L_M/\sqrt{3}[\sin(2\pi m/3)\hat{\boldsymbol{x}} + \cos(2\pi m/3)\hat{\boldsymbol{y}}], \tag{S8}$$

with $L_M = 0.246$ nm$/(2\sin\theta/2)$, and a narrow bandwidth W. The corresponding rescaled energies and Bloch states are

$$E_\nu(\boldsymbol{k}) = \nu|h_{\boldsymbol{k}}|, \tag{S9}$$

and

$$|\nu\boldsymbol{k}\rangle = \frac{1}{\sqrt{2}}\begin{pmatrix} \nu e^{i\arg(h_{\boldsymbol{k}})} \\ 1 \end{pmatrix}, \tag{S10}$$

respectively, with $\nu = \pm 1$ enumerating the narrow Bloch bands.

Following Ref. [2], we perform minimal coupling, which turns the functions $h_{\boldsymbol{k}}$ into time-dependent quantities with Fourier transforms

$$\begin{aligned} h^{(n)}_{\boldsymbol{k}} &= \frac{1}{2\pi/\Omega}\int_0^{2\pi/\Omega} h_{\boldsymbol{k}+e\boldsymbol{A}(t)/\hbar}e^{-in\Omega t}dt \\ &= \sum_j te^{i\boldsymbol{k}\cdot\boldsymbol{\delta}_j}e^{in\phi_j}J_n(-\tilde{\mathcal{E}}), \end{aligned} \tag{S11}$$

where $\tilde{\mathcal{E}}$ is the dimensionless drive strength

$$\tilde{\mathcal{E}} = \frac{eL_M}{\sqrt{3}\hbar}A = \frac{eL_M}{\sqrt{3}\hbar}\frac{\mathcal{E}}{\Omega}; \tag{S12}$$

the phase angles are $\phi_0 = \pi/2$, $\phi_1 = -5\pi/6$, and $\phi_2 = -\pi/6$; and

$$J_n(z) = \frac{1}{2\pi i^n}\int_0^{2\pi} e^{iz\cos\theta}e^{in\theta}d\theta. \tag{S13}$$

The Fourier-transformed Hamiltonian is

$$H^{(n)}_{\text{toy}}(\boldsymbol{k}) = \begin{pmatrix} 0 & h^{(n)}_{\boldsymbol{k}} \\ h^{*(n)}_{\boldsymbol{k}} & 0 \end{pmatrix}. \tag{S14}$$

Note that

$$h^{*(n)}_{\boldsymbol{k}} = \sum_j te^{-i\boldsymbol{k}\cdot\boldsymbol{\delta}_j}e^{in\phi_j}J_n(\tilde{\mathcal{E}}) \tag{S15}$$

is the Fourier transform of the conjugate of $h_{\boldsymbol{k}}$. In simulations, we generally truncate the Fourier Hamiltonian (Eq. S5) to $-12 \le m \le 12$, so that we account for a sufficient number of high-order Floquet-Umklapp processes in the Floquet-Boltzmann equation. We do not perform the gauge transformation $h^{(n)}_{\boldsymbol{k}} \to ie^{-i\boldsymbol{k}\cdot\boldsymbol{\delta}_0}h^{(n)}_{\boldsymbol{k}}$ so as to preserve the C_3 symmetry of the matrix element in the Floquet-Boltzmann equation (see Eq. S78).

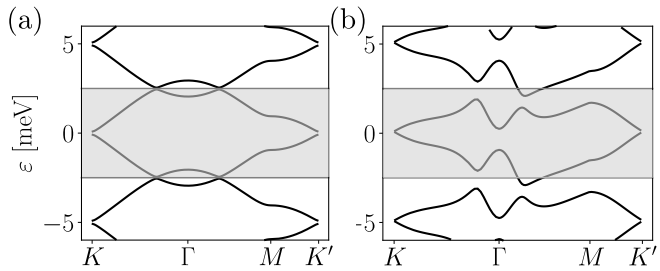

FIG. S1. (a) The quasienergy band structure of the toy model with for the parameters used in the main text. (b) The quasienergy band structure of the continuum model at valley $\xi = +1$. In both panels, the first Floquet Brillouin zone is shaded. See Sec. II for details and justification for the parameters we have used.

B. Continuum Model Floquet Hamiltonian

The undriven continuum model for TBG [3] describes the bandstructure of TBG near the valley $\xi = \pm 1$ of the monolayer graphene Brillouin zone. Its Hamiltonian

$$H_\xi(\boldsymbol{k}) = \begin{pmatrix} H_1^\xi(\boldsymbol{k}) & U_\xi^\dagger \\ U_\xi & H_2^\xi(\boldsymbol{k}) \end{pmatrix} \tag{S16}$$

is diagonalized in the basis $\psi_{n\boldsymbol{k}} = (\psi_{n\boldsymbol{k}}^{A_1}, \psi_{n\boldsymbol{k}}^{B_1}, \psi_{n\boldsymbol{k}}^{A_2}, \psi_{n\boldsymbol{k}}^{B_2})^T$ with

$$\psi_{n\boldsymbol{k}}^X(\boldsymbol{r}) = e^{i\boldsymbol{k}_{\rm mic}\cdot\boldsymbol{r}} \sum_{\boldsymbol{G}} C_{n\boldsymbol{k}}^X(\boldsymbol{G}) e^{i\boldsymbol{G}\cdot\boldsymbol{r}} \tag{S17}$$

where $X = A_l, B_l$ represents sublattice A or B degree of freedom in layer index $l = \pm 1$, $\boldsymbol{k}_{\rm mic} = \boldsymbol{k} + (\boldsymbol{K}_\xi^{+1} + \boldsymbol{K}_\xi^{-1})/2 + \hat{\boldsymbol{x}}\sqrt{3}\xi/2|\boldsymbol{K}_\xi^{+1} - \boldsymbol{K}_\xi^{-1}|$ is the microscopic momentum of the electrons, $\boldsymbol{k}$ is the mini Brillouin zone momentum, and

$$\boldsymbol{K}_\xi^l = -\xi \frac{4\pi}{3a} R(-l\theta/2)\hat{\boldsymbol{x}} \tag{S18}$$

for layer $l = \pm 1$ and $a = 0.246$ nm. In Eq. S16, H_l^ξ are the monolayer graphene Hamiltonians, which, in close vicinity of the $\xi = \pm 1$ valleys, resemble Dirac cones:

$$H_l^\xi(\boldsymbol{k}) = -\hbar v_F^{\rm ml} \left[R(l\theta/2)(\boldsymbol{k}_{\rm mic} - \boldsymbol{K}_\xi^l) \right] \cdot (\xi\sigma_x, \sigma_y) \tag{S19}$$

where $R(\varphi)$ is the 2×2 rotation matrix, and $v_F^{\rm ml}$ is the monolayer Graphene Fermi velocity. The interlayer coupling is

$$U_\xi = \begin{pmatrix} u & u' \\ u' & u \end{pmatrix} + \begin{pmatrix} u & u'\nu^{-\xi} \\ u'\nu^{\xi} & u \end{pmatrix} e^{i\xi\boldsymbol{G}_1\cdot\boldsymbol{r}} + \begin{pmatrix} u & u'\nu^{\xi} \\ u'\nu^{-\xi} & u \end{pmatrix} e^{i\xi(\boldsymbol{G}_2+\boldsymbol{G}_3)\cdot\boldsymbol{r}} \tag{S20}$$

Using minimal coupling, we obtain time-dependent monolayer graphene Hamiltonians, with Fourier transform

$$H_l^{\xi(n)}(\boldsymbol{k}) = -\hbar v \Big\{ R(l\theta/2) \Big([\boldsymbol{k}_{\rm mic} - \boldsymbol{K}_\xi^{(l)}]\delta_{n,0} + \frac{e}{\hbar}\frac{1}{2}\mathcal{E}[(\delta_{n,1} + \delta_{n,-1})\hat{\boldsymbol{y}} - i(\delta_{n,-1} - \delta_{n,1})\hat{\boldsymbol{x}}] \Big) \Big\} \cdot (\xi\sigma_x, \sigma_y). \tag{S21}$$

Then,

$$H_\xi^{(n)} = \begin{pmatrix} H_1^{\xi(n)}(\boldsymbol{k}) & U_\xi^\dagger \delta_{n,0} \\ U_\xi \delta_{n,0} & H_2^{\xi(n)}(\boldsymbol{k}) \end{pmatrix} \tag{S22}$$

is the Fourier transform of the continuum model Hamiltonian. For the continuum model, we truncate the Floquet Hamiltonian (Eq. S16) to $-6 \le m \le 6$.

Upon diagonalizing the Floquet Hamiltonian, we obtain a large number of Floquet states per energy interval $[-\hbar\Omega/2, \hbar\Omega/2]$. We select two states per $\boldsymbol{k}$-point whose spectral weights $A_\alpha^0(\boldsymbol{k}) = |\langle\phi_{\boldsymbol{k}\alpha}^0|\phi_{\boldsymbol{k}\alpha}^0\rangle|^2$ are large (which makes their contribution to the Floquet-Boltzmann equation most important, see Sec. X).

C. Quasienergy Bands

In Sec. II, we provide and motivate the choices of physical parameters that we use in the main text. In Fig. S1, we preview the quasienergy bands for our choice of toy and continuum model parameters.

II. CHOICE OF PHYSICAL PARAMETERS

First, we present the physical parameters we use for the electronic Hamiltonian in the TBG continuum model (see Sec. I B for the Hamiltonian). We consider the non-interacting continuum model [3, 4] at a near-magic twist angle of $\theta = 1.13°$. The bandwidth of the central bands at this angle is $W \approx 5$ meV, and a perturbative expansion of the Hamiltonian around the Brillouin zone Dirac points [4] estimates the Fermi velocity as

$$v_F(\theta) = v_F^{\rm ml}(1 - 3\beta^2)/(1 + 3\beta^2(1+\eta^2)), \tag{S23}$$

where $\beta = u'/(\hbar k_\theta v_F^{\rm ml})$ and $\eta = u/u'$ with $v_F^{\rm ml} = 8\times 10^5$ m/s, $k_\theta = 4\pi/(3L_M)$, $u = 0.0797$ eV, and $u' = 0.0975$ eV [3, 4]. Eq. S23 predicts that the Fermi velocity at the chosen twist angle is $v_F = 27$ km/s. However, the derivation of Eq. S23 approximates that H_l^ξ is roughly θ-independent and tends to overestimate v_F (see Fig. 4 inset in [4]). We can obtain a better estimate by numerically calculating the Fermi velocity along the path K-M in $\boldsymbol{k}$-space of the $\nu = +1$ band in the $\xi = +1$ valley.

(This is the direction of maximum Fermi velocity.) The estimate yields $v_F = 17.5$ km/s, and we hereafter use this value. In our Floquet Hamiltonian, we use a laser angular-frequency of $\Omega \approx W/\hbar \approx 5$ meV/$\hbar$.

Second, we present the parameters we use for the electronic Hamiltonian of the TBG two-band toy tight binding model (see Sec. I A for the Hamiltonian). We choose our toy model Fermi velocity, frequency, and twist angle to roughly match those of the continuum model. Specifically, we use a twist angle of $\theta = 1.13°$ and choose $W = 3.1$ meV so that the Fermi velocity $v_F = WL_M/(2\sqrt{3}\hbar) = 17$ km/s roughly matches that of the continuum model at the same angle. In the toy model Floquet Hamiltonian, we choose $\Omega \approx 5$ meV/$\hbar$.

Third, we discuss the parameters we use for the TBG phonons. For both the continuum and toy models, we consider phonons speeds in the range of $c_{\rm ph} \in [17.9 \text{ km/s}, 19.4 \text{ km/s}]$. In the toy model, $v^0_{\rm eff} = 18.9$ km/s, and, in the continuum model, $v^0_{\rm eff} = 19.5$ km/s, so the range of $c_{\rm ph}$ we choose covers the regime $c_{\rm ph} < v^0_{\rm eff}$, in which the drive induces the opposite regime $c_{\rm ph} > v_{\rm eff}(\mathcal{E})$ when $\mathcal{E} > \mathcal{E}^*$. We also use the same phonon bath temperature of $T_{\rm ph} = 1$ K for the toy and continuum model calculations.

Please see Sec. XV for details of the numerical $\boldsymbol{k}$-point grid and Sec. XII for details of the toy model form factor.

III. ANOMALOUS HALL CONDUCTIVITY CALCULATIONS FOR THE CONTINUUM MODEL

In this section, we repeat the calculations in the main text on the TBG continuum model [3, 4]. We consider the non-interacting limit, setting $\epsilon \to \infty$ so that $I^{\text{el-el}}_{\boldsymbol{k}\alpha} = 0$.

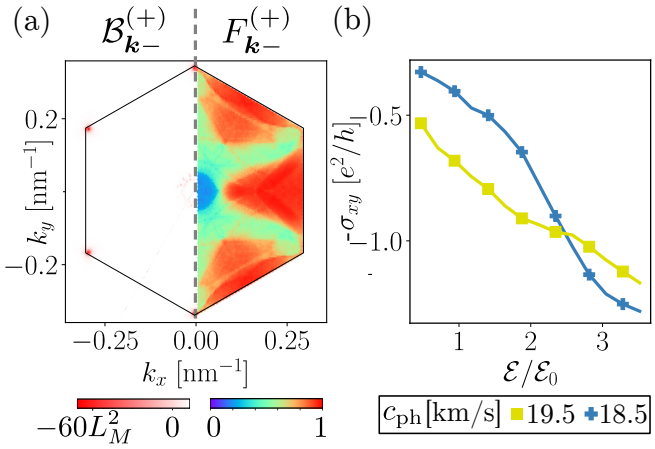

FIG. S2. (a) Left: the steady-state occupation of the lower Floquet band in valley $\xi = +1$ of the continuum model [3, 4]. Right: the Berry curvature of the same band, which peaks near the Dirac points and the resonance ring. (b) The anomalous Hall conductivity σ_{xy} as a function of drive strength $\mathcal{E}$.

First, we discuss differences in the bandstructure and topology at valleys $\xi = +$ and $\xi = -$. The circularly polarized laser opens a gap at the Dirac points, Δ_K, effectively adding a mass term $\xi\Delta_K\sigma_z$ to the Hamiltonian (see Sec. I B and [5] for a derivation) in the vicinity of the Dirac points. Because the sign of the mass term depends on ξ, the $\xi = \pm 1$ superlattice valley contributions to σ_{xy} do not trivially cancel to zero. In fact, in reciprocal space, the Berry curvature and occupations near $\xi = +1$ are simple $\pi/3$ rotations of those in $\xi = -1$, so

$$\sigma_{xy} = \frac{4e^2}{h} \sum_{\alpha=\pm} \int_{\rm MBZ} \frac{d^2\boldsymbol{k}}{(2\pi)^2} \mathcal{B}^{(+1)}_{\boldsymbol{k}\alpha} F^{(+1)}_{\boldsymbol{k}\alpha}. \tag{S24}$$

In Fig. S2, we show the steady-state and σ_{xy} for the continuum model calculation. Note that we use the full form factor $\mathcal{W}^{\xi\nu'\nu}_{\boldsymbol{k},\boldsymbol{q}} = \langle \xi\nu'\boldsymbol{k} + \boldsymbol{q} | \xi\nu\boldsymbol{k}\rangle$ as calculated from the continuum model wavefunctions (see Sec. XII).

IV. DIRECT VARIATION OF THE PHONON SPEED $c_{\rm ph}$

Throughout the main text, we use the drive strength $\mathcal{E}$ to control electron speeds. We could achieve similar results by keeping $\mathcal{E}$ fixed and varying $c_{\rm ph}$ instead. Fig. S3 shows the variation of σ_{xy} as a function of $c_{\rm ph}$. The curves resemble the dependence of σ_{xy} on $\mathcal{E}$ in the main text (see, for e.g., Fig. 1(b)).

V. SYMMETRIES AND BERRY CURVATURE DISTRIBUTIONS OF THE TOY AND CONTINUUM MODELS

In this section, we compare the symmetries of the toy and continuum models with and without the drive, and we show that the Berry curvature distributions of the models with the drive are consistent near the Dirac points.

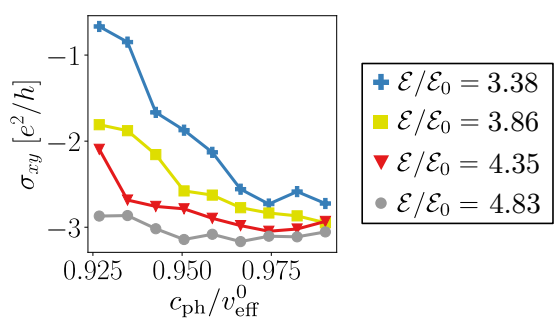

FIG. S3. Anomalous Hall conductivity of the toy model as a function of the ratio $c_{\rm ph}/v^0_{\rm eff}$ for three different drive field strengths $\mathcal{E}/\mathcal{E}_0$. The same electron-phonon decoupling process is visible as σ_{xy} plateaus.

A. Symmetries

The symmetries of the undriven BM continuum model are $C_{2z}T = \sigma_x\mathcal{K}$, $C_3 = e^{i2\pi/3\sigma_z}$, and $C_{2x} = \sigma_x\tau_x$, where τ_i and σ_i are in the layer and sublattice degrees of freedom, $i = 0, x, y, z$, and $\mathcal{K}$ is conjugation. At charge neutrality, undriven TBG also has an emergent, approximate unitary particle-hole symmetry $P = i\tau_y$ and anti-unitary particle-hole symmetry $\mathcal{P} = PC_{2z}T$ within each superlattice valley, which ensures $PH_\xi(\boldsymbol{k})P^{-1} \approx -H_\xi(-\boldsymbol{k})$ and $\mathcal{P}H_\xi(\boldsymbol{k})\mathcal{P}^{-1} \approx -H_\xi(-\boldsymbol{k})$ (see Eq. S16 for the definition of $H_\xi(\boldsymbol{k})$) [6–8].

We now discuss the effect of the drive on the symmetries of the BM model. The drive induces a dynamical Haldane mass term $\Delta_K\xi\sigma_z$ (see Sec. V B). It also resonantly-couples states around the resonance ring, where the effective Hamiltonian is

$$H_R^\xi(\boldsymbol{k}) = V_R(\boldsymbol{k})|\xi-\boldsymbol{k}\rangle\langle\xi+\boldsymbol{k}| + V_R^*(\boldsymbol{k})|\xi+\boldsymbol{k}\rangle\langle\xi-\boldsymbol{k}| \quad \text{(S25)}$$

as derived from degenerate perturbation theory, where $V_R(\boldsymbol{k}) = \langle\xi-\boldsymbol{k}|H_\xi^{(1)}(\boldsymbol{k})|\xi+\boldsymbol{k}\rangle$ and $|\xi\pm\boldsymbol{k}\rangle$ are the undriven single-particle Bloch states (see the main text for the definition) [9]. We can see that the drive breaks $C_{2z}T$ symmetry by opening the Haldane gap. The drive also breaks P symmetry because the drive-induced Haldane mass term $\Delta_K\xi\sigma_z$ commutes with P. However, the drive preserves the anti-unitary $\mathcal{P}$ symmetry. One can see this by first noting that $(C_{2z}T)\sigma_z(C_{2z}T)^{-1} = -\sigma_z$, so $\mathcal{P}\Delta_K\xi\sigma_z\mathcal{P}^{-1} = -\Delta_K\xi\sigma_z$. Secondly, since $\mathcal{P}|\xi-,\pm\boldsymbol{k}\rangle = |\xi+,\mp\boldsymbol{k}\rangle$,

$$\begin{aligned}\mathcal{P}H_R(\boldsymbol{k})\mathcal{P}^{-1} = V_R(\boldsymbol{k})|\xi+,-\boldsymbol{k}\rangle\langle\xi-,-\boldsymbol{k}| \\ + V_R^*(\boldsymbol{k})|\xi-,-\boldsymbol{k}\rangle\langle\xi+,-\boldsymbol{k}|.\end{aligned} \quad \text{(S26)}$$

Noting that $\mathcal{P}H_\xi^{(1)}(\boldsymbol{k})\mathcal{P}^{-1} = -H_\xi^{(-1)}(-\boldsymbol{k})$ and $|\xi+\boldsymbol{k}\rangle = \mathcal{P}^{-1}|\xi-,-\boldsymbol{k}\rangle$, we find that

$$V_R(\boldsymbol{k}) = -\langle\xi+,-\boldsymbol{k}|H_\xi^{(-1)}(-\boldsymbol{k})|\xi-,-\boldsymbol{k}\rangle = -V_R^*(-\boldsymbol{k}). \quad \text{(S27)}$$

Therefore, $\mathcal{P}H_R(\boldsymbol{k})\mathcal{P}^{-1} = -H_R(-\boldsymbol{k})$, and the Hamiltonian is also particle-hole symmetric along the resonantly-coupled states. Lastly, the drive preserves C_3 symmetry and C_{2x} symmetry, which one can see by noting the following:

$$C_3H_\xi(\boldsymbol{k})C_3^{-1} = H_\xi(\boldsymbol{k}),\ C_{2x}H_\xi(\boldsymbol{k})C_{2x}^{-1} = H_{-\xi}(\boldsymbol{k}), \quad \text{(S28)}$$

$$C_3\Delta_K\xi\sigma_zC_3^{-1} = \Delta_K\xi\sigma_z,\ C_{2x}\Delta_K\xi\sigma_zC_{2x}^{-1} = -\Delta_K\xi\sigma_z, \quad \text{(S29)}$$

and

$$C_3H_R^\xi(\boldsymbol{k})C_3^{-1} = H_R^\xi(\boldsymbol{k}),\ C_{2x}H_R^\xi(\boldsymbol{k})C_{2x}^{-1} = H_R^{-\xi}(\boldsymbol{k}). \quad \text{(S30)}$$

Thus, the Hamiltonian near the Dirac points and resonantly-coupled states respect the C_3 and C_{2x} symmetries.

Now, we discuss the symmetries of the toy model. In the undriven limit, the toy model has exact particle-hole symmetry $P = \sigma_z\mathcal{K}$. It also has the symmetries $C_{2z}T = \sigma_x\mathcal{K}$, $C = \sigma_z$ (sublattice/chiral symmetry), and $C_3 = e^{i2\pi/3\sigma_z}$. The drive opens a Haldane mass gap $\Delta_K\xi_{\text{MBZ}}\sigma_z$, where $\xi_{\text{MBZ}} = 1$ (-1) for the mini Brillouin zone K (K') point. We can now see that the drive breaks $C_{2z}T$, C, and T symmetry via the Haldane mass term, while preserving $P = CT$ symmetry. One can see that P is preserved by noting that $P\Delta_K\xi_{\text{MBZ}}\sigma_zP^{-1} = -\Delta_K\xi_{\text{MBZ}}\sigma_z$ since conjugation $\mathcal{K}$ inverts the momentum and hence the sign of the mass term. Similar arguments as the continuum model case can be made to show that the Hamiltonian near the resonance ring respects P.

Importantly, the drive preserves the emergent particle-hole symmetry in the continuum model while preserving the exact particle-hole symmetry in the toy model. As we note in the phenomenological analysis section of the main text, the emergent particle-hole symmetry ensures that the electron and hole scattering rates in the UFB and LFB are similar. Secondly, the drive breaks $C_{2z}T$ symmetry in both models by opening a Haldane gap. In Sec. V B, we show that the Haldane gap ensures the Berry curvature distributions of the models near the Dirac points are consistent.

B. Berry Curvature

The tunable conductivity σ_{xy} relies only on the large Berry curvature and electron-phonon scattering bottlenecks near the Dirac points of the mini Brillouin zone. In this section, we detail how the Berry curvature distributions for the toy and continuum models are consistent near the Dirac points, as the numerical calculations of Berry curvature demonstrate in Fig. S4. We now prove the agreement analytically. The Hamiltonian for the mini Brillouin zone Dirac cone in the toy model is given by

$$H_{\text{Dirac}}^{\text{toy}}(\boldsymbol{q}) = \hbar v_F\boldsymbol{q}\cdot(\xi_{\text{MBZ}}\sigma_x, \sigma_y), \quad \text{(S31)}$$

where $\boldsymbol{q}$ is the momentum measured from the K or K' point, v_F is the Fermi velocity of TBG, and $\xi_{\text{MBZ}} = +$ for the K point and $\xi_{\text{MBZ}} = -$ for the K' point in the mini Brillouin zone. The corresponding Hamiltonian for the continuum model is

$$H_{\text{Dirac}}^{\text{cont}}(\boldsymbol{q}) = \hbar v_F\boldsymbol{q}\cdot(\xi\sigma_x, \sigma_y) \quad \text{(S32)}$$

where ξ is the superlattice valley index. Upon applying minimal coupling and the Van-Vleck perturbative expansion (see Sec. X for details), one finds the effective Floquet Hamiltonians

$$H_{\text{Dirac,eff}}^{\text{toy}}(\boldsymbol{q}) = \hbar v_F\boldsymbol{q}\cdot(\xi_{\text{MBZ}}\sigma_x, \sigma_y) + \xi_{\text{MBZ}}\Delta_K\sigma_z \quad \text{(S33)}$$

$$H_{\text{Dirac,eff}}^{\text{cont}}(\boldsymbol{q}) = \hbar v_F\boldsymbol{q}\cdot(\xi\sigma_x, \sigma_y) + \xi\Delta_K\sigma_z. \quad \text{(S34)}$$

We note that in both models, the Berry curvature does not alternate signs between the K and K' points in mini Brillouin zone. Additionally, Eq. S34 shows that the drive breaks time-reversal symmetry between the superlattice valleys $\xi = \pm 1$ in the BM model, permitting nonzero σ_{xy} when contributions to the conductivity from both superlattice valleys are combined.

VI. FULL PHENOMENOLOGICAL MODEL

In this section, we derive a detailed phenomenological model that qualitatively reproduces the dependence of σ_{xy} on $\mathcal{E}$ and the effect of interactions presented in the main text.

Let us begin by adding more details to the phenomenological model for the K-point occupation. We write

$$\begin{aligned} F_{K+}^{(\xi)} = [&\mathcal{R}_{\text{in}} F_+ + \Gamma_{\text{in}}^{\text{el}} + \Gamma_{\text{in}}^{\text{el,FU}} + \mathcal{R}_{\text{in}}^{\text{FU}} F_-]/ \\ &[\mathcal{R}_{\text{in}} F_+ + \mathcal{R}_{\text{out}}(1 - F_-) \\ &+ \Gamma_{\text{in}}^{\text{el}} + \Gamma_{\text{in}}^{\text{el,FU}} + \Gamma_{\text{out}}^{\text{el}} + \Gamma_{\text{out}}^{\text{el,FU}} \\ &+ \mathcal{R}_{\text{in}}^{\text{FU}} F_- + \mathcal{R}_{\text{out}}^{\text{FU}}(1 - F_+)], \end{aligned} \tag{S35}$$

where $\Gamma_{\text{in/out}}^{\text{el}}$, $\Gamma_{\text{in/out}}^{\text{el, FU}}$ and $\mathcal{R}_{\text{in/out}}^{\text{FU}}$ are the non-FU electron-electron, FU electron-electron, and FU electron-phonon scattering rates, respectively. Here, F_α is the average occupation of Floquet band α outside the resonance ring, and $F_+ = 1 - F_-$. We drop the superscript (ξ) on the occupations for simplicity and work within a single superlattice valley. Let us now make the following approximations and definitions:

$$\Gamma_{\text{in}}^{\text{el}} \approx \Gamma_{\text{out}}^{\text{el}} \equiv \Gamma, \text{ and } \Gamma_{\text{in}}^{\text{el,FU}} \approx \Gamma_{\text{out}}^{\text{el,FU}} \approx S\Gamma, \tag{S36}$$

where FU processes are suppressed by a factor of $S \equiv (V/\hbar\Omega)^2$, with $V \approx v_F e\mathcal{E}/\Omega$. For phonon transitions, let us make the following definitions:

$$\mathcal{R}_{\text{out}} \equiv \mathcal{R}, \text{ and } \mathcal{R}_{\text{in}} = r\mathcal{R}, \tag{S37}$$

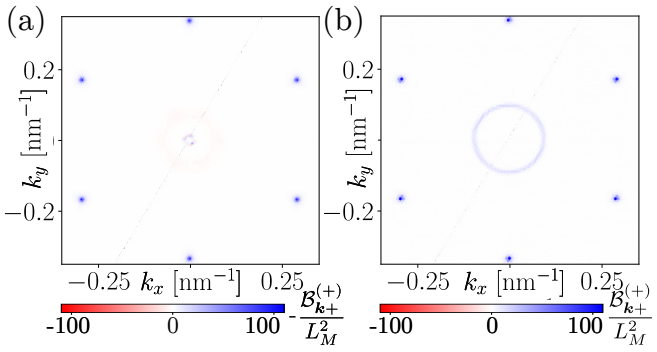

FIG. S4. Comparing the Berry curvature distribution in the upper Floquet band in the (a) continuum model and (b) toy model at a drive amplitude of $\mathcal{E}/\mathcal{E}_0 \approx 3.1$.

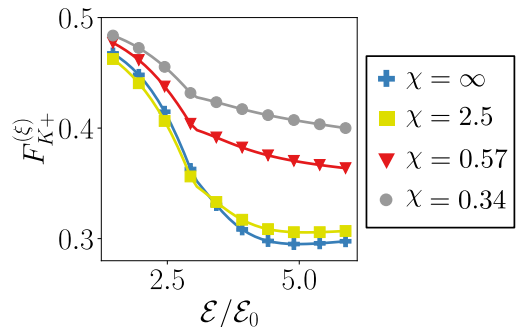

FIG. S5. The occupation $F_{K+}^{(\xi)}$ as predicted by the phenomenological model in Sec. VI for different ratios $\chi \equiv \tau_K^{\text{el}}/\tau_K^{\text{ph}}$. Note that for large χ, the occupation is *lower* than the non-interacting case at weak drive amplitudes, an effect of reduced Pauli blocking in the electron-phonon interactions.

where $r \equiv \mathcal{R}_{\text{in}}/\mathcal{R}_{\text{out}}$. Let us also define $r^{\text{FU}} \equiv \mathcal{R}_{\text{in}}^{\text{FU}}/\mathcal{R}_{\text{out}}^{\text{FU}}$, and approximate $\mathcal{R}_{\text{out}}^{\text{FU}} \approx S a^{\text{FU}} \mathcal{R}$, where the factor $a^{\text{FU}} > 1$ accounts for the fact that the phase space area of states connected to the UFB K point by FU processes is much larger than area of states connected to the UFB K point by non-FU processes. We therefore obtain

$$\mathcal{R}_{\text{out}}^{\text{FU}} = S a^{\text{FU}} \mathcal{R}, \text{ and } \mathcal{R}_{\text{in}}^{\text{FU}} = S a^{\text{FU}} r^{\text{FU}} \mathcal{R}. \tag{S38}$$

Now, Eq. S35 reduces to

$$F_{K+}^{(\xi)} = \frac{r F_+ \mathcal{R} + S F_- a^{\text{FU}} r^{\text{FU}} \mathcal{R} + (1+S)\Gamma}{(1+r) F_+ \mathcal{R} + S(1 + r^{\text{FU}}) F_- a^{\text{FU}} \mathcal{R} + 2(1+S)\Gamma}. \tag{S39}$$

Let us further define $x \equiv \Gamma/\mathcal{R}$ as a ratio of electron-electron to electron-phonon scattering rates and use $F_- \approx 1 - F_+$ (ensured by emergent particle-hole symmetry, see Sec. V A) to obtain

$$F_{K+}^{(\xi)} = \frac{r F_+ + S(1 - F_+) a^{\text{FU}} r^{\text{FU}} + (1+S)x}{(1+r) F_+ + S(1 + r^{\text{FU}})(1 - F_+) a^{\text{FU}} + 2(1+S)x}. \tag{S40}$$

We will determine the dependence of $F_{K+}^{(\xi)}$ on interaction strength x at strong and weak drive amplitudes.

We now derive the phenomenological equation for F_α. The rate equation is roughly

$$\begin{aligned} \dot{F}_+ \approx &\Lambda_{\text{in}} F_-(1 - F_+) - \Lambda_{\text{out}} F_+(1 - F_-) \\ &+ \Gamma(1+S)(1 - F_+) - \Gamma(1+S) F_+ \end{aligned} \tag{S41}$$

where Λ_{in} and Λ_{out} are electron-phonon scattering rates into and out of the UFB. Note that $\Lambda_{\text{in}} \approx S\Lambda_{\text{out}}$ since scattering processes described by Λ_{in} are FU processes. We also approximate $\Lambda_{\text{out}} \approx f_b \mathcal{R}$, with a factor $f_b > 1$, because we expect $\mathcal{R}$, which is suppressed by strong electron-phonon scattering bottlenecks near the K point, to be smaller than Λ_{out}, the total scattering rate into the UFB. We can then find the steady-state solution F_+ in terms of x and substitute the results into Eq. S40.

In Fig. S5, we show the occupation $F_{K+}^{(\xi)}$ as a function of $\mathcal{E}$ for different values of $\chi = \tau_K^{\rm el}/\tau_K^{\rm ph} \approx x^{-1}F_+|_{\mathcal{E}=\mathcal{E}^*}$ (c.f. $1/\tau_K^{\rm ph} \sim \mathcal{R}F_+|_{\mathcal{E}=\mathcal{E}^*}$ and $1/\tau_K^{\rm el} \sim \Gamma$) where $F_+|_{\mathcal{E}=\mathcal{E}^*}$ is F_+ evaluated at the drive ampltiude $\mathcal{E}^*$, which we choose to be $\mathcal{E}^* = 2.5\mathcal{E}_0$. To generate the figure, we choose $f_b = 3$ and $a^{\rm FU} = 28$. Note that $a^{\rm FU}$ estimates that the total area of momentum states connected to $\mathcal{A}_K$ by electron-phonon FU processes covers roughly 1/6 of the Brillouin zone. We write the following $\mathcal{E}$-dependent phenomenological equations for the ratios r and $r^{\rm FU}$ that capture very roughly their dependence on $\mathcal{E}$, inspired by Fig. 4(b) in the main text. First, we approximate

$$r \approx \max\left[\frac{2}{e^{(\mathcal{E}-\mathcal{E}^*)/(0.8\mathcal{E}_0)}+1} - 1, 0\right]. \tag{S42}$$

Note $r \sim 1$ for $\mathcal{E} \ll \mathcal{E}^*$ and $r = 0$ for $\mathcal{E} > \mathcal{E}^*$, capturing the behavior shown in Fig. 4(b) in the main text. Second, we choose

$$r^{\rm FU} \approx \frac{1/2}{e^{(\mathcal{E}-\mathcal{E}^*)/(0.5\mathcal{E}_0)}+1} + \frac{1}{2}. \tag{S43}$$

Here, $r^{\rm FU} \sim 1$ for $\mathcal{E} \ll \mathcal{E}^*$ and decreases with $\mathcal{E}$, but never reaches 0 (since the electrons are never decoupled from electron-phonon FU processes).

Two features are notable in Fig. S5. First, the occupation decreases as a function of interaction strength for weak interactions (large χ) and weak drive amplitudes, a result of interactions reducing Pauli blocking of the phonon processes from patch $\mathcal{S}_{\rm in}$ to $\mathcal{S}_K$ and from $\mathcal{S}_K$ to $\mathcal{S}_{\rm out}$ (i.e., increasing $F_{\rm in}^{(\xi)}$ in Eq. 6 of the main text, correspondingly suppressing $F_{K+}^{(\xi)}$). When interactions are strong (small χ), $\Gamma_{\rm in/out}^{\rm el}$ dominates, and $F_{K+}^{(\xi)} \to 0.5$. Second, the occupation increases slowly for $\mathcal{E} > \mathcal{E}^*$, since FU processes strengthen as $(V/\hbar\Omega)^2$ grows with $\mathcal{E}$. Both of these behaviors are visible in Fig. 3(c) in the main text.

VII. FORMAL DEFINITION, NUMERICAL EVALUATION, AND PHENOMENOLOGICAL MODEL OF $\mathcal{A}_{\rm in}$

As described in the main text, a patch $\mathcal{S}_{\rm in}$ shaped as an elliptical annulus (see Fig. 3(a)) with area $\mathcal{A}_{\rm in}$ in momentum space vanishes as $\mathcal{E} \to \mathcal{E}^*$. Here, we provide a formal definition of $\mathcal{A}_{\rm in}$ and explain how we estimate its dependence on $\mathcal{E}$ numerically and analytically.

A. Formal Definition

Let us first define $\mathcal{A}_{\rm in}$ formally. Consider a family of phonon cones centered throughout $\mathcal{S}_K$, the circular patch enclosing a K-point in the quasienergy spectrum (see Fig. 3(a)). Suppose that a subset of the phonon cones are centered throughout a small quasienergy window $d\varepsilon_{\boldsymbol{k}+}$. The $\boldsymbol{k}$-space area of states $d\mathcal{A}_{\rm in}$ containing intersections of the cones with the upper Floquet band is

$$d\mathcal{A}_{\rm in} = d\varepsilon_{\boldsymbol{k}+}\sum_{s=\pm}\int d^2\boldsymbol{k}'\ \delta(\varepsilon_{\boldsymbol{k}+} - \varepsilon_{\boldsymbol{k}'+} + s\hbar c_{\rm ph}|\boldsymbol{k}'-\boldsymbol{k}|). \tag{S44}$$

Next, we integrate over $\varepsilon_{\boldsymbol{k}+}$ contained in $\mathcal{S}_K$ to obtain

$$\mathcal{A}_{\rm in} = \int d\mathcal{A} = \int_{\boldsymbol{k}\in\mathcal{S}_K} d^2\boldsymbol{k}\frac{1}{D(\varepsilon_{\boldsymbol{k}+})}\times \times\left[\sum_{s=\pm}\int d^2\boldsymbol{k}'\ \delta(\varepsilon_{\boldsymbol{k}+} - \varepsilon_{\boldsymbol{k}'+} + s\hbar c_{\rm ph}|\boldsymbol{k}'-\boldsymbol{k}|)\right], \tag{S45}$$

where

$$D(\varepsilon) = \sum_\alpha\int\frac{d^2\boldsymbol{k}}{(2\pi)^2}\delta(\varepsilon - \varepsilon_{\boldsymbol{k}\alpha}) \tag{S46}$$

is the density of states in the quasienergy band structure. Exploiting the circular shape of $\mathcal{S}_K$,

$$\int_{\boldsymbol{k}\in\mathcal{S}_K} d^2\boldsymbol{k} \approx \int d^2\boldsymbol{k}\ \Theta(|\boldsymbol{k}-\boldsymbol{K}| - k_p) \tag{S47}$$

where k_p is the radius of the circular area $\mathcal{A}_K$ of $\mathcal{S}_K$. Lastly, we calculate an approximate expression for k_p, the radius of $\mathcal{A}_K$. In the vicinity of the Dirac cone, the Hamiltonian is

$$H_K(\boldsymbol{k},t) = \boldsymbol{d}\cdot\boldsymbol{\sigma}, \tag{S48}$$

where $\boldsymbol{d} = \hbar v_F\xi k_x\hat{\boldsymbol{x}} + \hbar v_F k_y\hat{\boldsymbol{y}} + \xi\Delta_K\mathcal{E}^2\hat{\boldsymbol{z}}$. (See Sec. X for a detailed derivation.) The $\boldsymbol{z}$-component of the Berry curvature is

$$\mathcal{B}_{k\alpha}^z = \alpha\frac{d_z}{2|\boldsymbol{d}|^3} = \alpha\frac{\Delta_K}{[(\hbar v_F k)^2 + \Delta_K^2]^{3/2}} \tag{S49}$$

where $d_z = \xi\Delta_K$ and $\alpha = \pm$. At the half-maximum, $\mathcal{B}_{k_p\alpha}^z = 0.5\mathcal{B}_{0\alpha}^z$, so

$$k_p = (2^{2/3}-1)^{1/2}\frac{\Delta_K}{\hbar v_F}. \tag{S50}$$

B. Numerical Estimate

To generate the values of $\mathcal{A}_{\rm in}$ we present in Fig. 3(b), we evaluate the integrals in Eq. S45 on a finite-sized grid of $\boldsymbol{k}$-points, smearing the step function by replacing $\Theta(|\boldsymbol{k}-\boldsymbol{K}|-k_p) \to [e^{(|\boldsymbol{k}-\boldsymbol{K}|-k_p)/\sigma_k}+1]^{-1}$, where $\sigma_k = 2\pi/(L_M N)$ is the grid spacing between $\boldsymbol{k}$-points on an $N\times N$ Monkhorst-Pack grid (see Sec. XV). Thus, we approximate

$$\mathcal{A}_{\rm in} \approx \sum_{\boldsymbol{k}}[e^{(|\boldsymbol{k}-\boldsymbol{K}|-k_p)/\sigma_k}+1]^{-1}\frac{1}{D(\varepsilon_{\boldsymbol{k}+})}\times \times\left[\sum_{s=\pm}\sum_{\boldsymbol{k}'}\ \delta(\varepsilon_{\boldsymbol{k}+} - \varepsilon_{\boldsymbol{k}'+} + s\hbar c_{\rm ph}|\boldsymbol{k}'-\boldsymbol{k}|)\right]. \tag{S51}$$

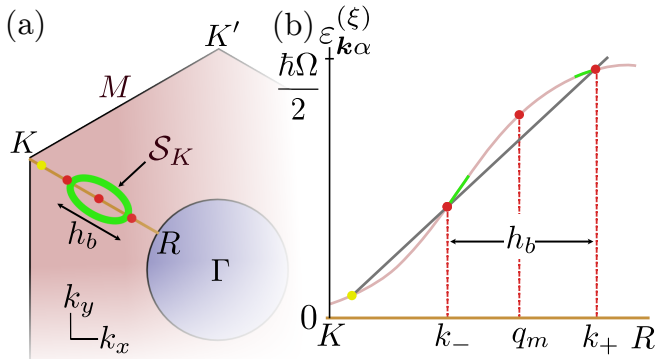

FIG. S6. (a) The intersection $\mathcal{S}_K$ (Fig. 3(a)) as viewed on the Brillouin zone. The outer radius along the path KR is $h_b(\mathcal{E})$. (b) Quasienergy (pink) along the path KR, with the phonon light cone (grey) that determines the *outer* radius of $\mathcal{A}_{\text{in}}$. The intersections k_+ and k_- between the cone and the upper Floquet band determines $h_b(\mathcal{E}) = k_+ - k_-$.

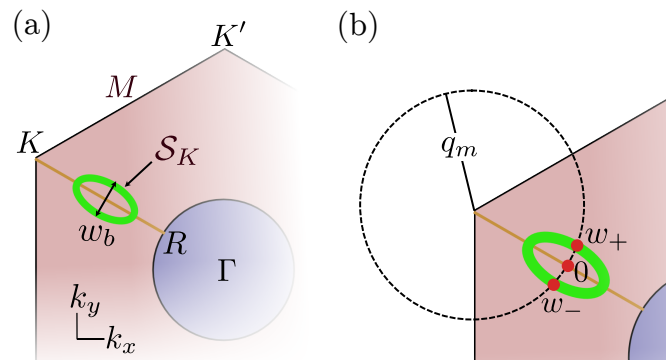

FIG. S7. (a) Width of the intersection $\mathcal{S}_K$, $w_b(\mathcal{E})$. (b) Circular coordinate system with arc length w (increasing counter-clockwise) that we use to determine $w_b(\mathcal{E}) = w_+ - w_-$.

For more information on how we approximate the Dirac Delta function on the grid, please see Sec. XV A. Note that we numerically-estimate the K-point occupation in a similar way, by calculating

$$F^{(\xi)}_{K+} \approx \sum_{\boldsymbol{k}} [e^{(|\boldsymbol{k}-\boldsymbol{K}|-k_p)/\sigma_k} + 1]^{-1} F^{(\xi)}_{\boldsymbol{k}+}. \tag{S52}$$

C. Phenomenological Model

In this section, we prove that the intersection area $\mathcal{A}_{\text{in}} \propto \max(\mathcal{E}^* - \mathcal{E}, 0)$ as $\mathcal{E} \to \mathcal{E}^*$. The shape of $\mathcal{A}_{\text{in}}$ is an elliptical annulus as shown in Fig. 3(a). Let us use $h_b(\mathcal{E})$ and $w_b(\mathcal{E})$ respectively to denote the *outer* major and minor axis radii of the elliptical annulus (see Figs. S6(a) and S7(a)). In the following sections, we begin by generating analytical estimates of $h_b(\mathcal{E})$ and $w_b(\mathcal{E})$.

1. *Estimate of h_b*

First, let us consider a slice of the upper Floquet band in $\boldsymbol{k}$-space from the K to the resonance ring (R) along the direction of $h_b(\mathcal{E})$, as we show in Fig. S6(b). Let us define a one-dimensional momentum component q along the path K-R. We sketch a phonon light cone (grey) originating from a point (yellow) in $\mathcal{S}_K$ that determines the outer radius of $\mathcal{A}_{\text{in}}$. The phonon cone intersects with the quasienergy at points k_+ and k_-, and the outer radius of $\mathcal{A}_{\text{in}}$ is therefore $h_b(\mathcal{E}) = k_+ - k_-$. First, consider the undriven limit $\mathcal{E} = 0$, where the gaps $\Delta_R = 0$ and $\Delta_K = 0$. We choose some point q_m such that $k_- < q_m < k_+$ and series expand the energy $E(q)$ of the undriven system around q_m:

$$\begin{aligned} E(q) &\approx E(q_m) + E'(q_m)(q - q_m) + \frac{1}{2}E''(q_m)(q - q_m)^2 \\ &= a_2 q^2 + a_1 q + a_0, \end{aligned} \tag{S53}$$

where $a_2 = E''(q_m)/2$, $a_1 = E'(q_m) - E''(q_m)q_m$, and $a_0 = E(q_m) - E'(q_m)q_m + E''(q_m)q_m^2/2$. As we increase $\mathcal{E}$, the gaps Δ_K and Δ_R widen. Let us write the quasienergy in the vicinity of q_m as

$$\varepsilon(q) \approx f(\mathcal{E})E(q) + \frac{\Delta_K}{2} \tag{S54}$$

where $f(\mathcal{E}) \leq 1$ is a scaling factor that decreases as $\mathcal{E}$ increases and accounts for band flattening due to Δ_K and Δ_R. Let

$$f^{-1} = 1 - b_1\tilde{\mathcal{E}} - b_2\tilde{\mathcal{E}}^2, \tag{S55}$$

where $b_1 \geq 0$ and $b_2 \geq 0$ are constants dependent on the exact bandstructure (i.e., how the widening of Δ_K and Δ_R with $\mathcal{E}$ affects the bandstructure near q_m). The roots of the equation $E(q) = \Delta_K/2 + \hbar c_{\text{ph}} q$ are $k_\pm$, and we may write the equation as

$$a_2 q^2 + a_1 q + a_0 = f\hbar c_s q, \tag{S56}$$

from which we find that

$$h_b = k_+ - k_- = \sqrt{(a_1 - f\hbar c_s)^2 - 4a_2 a_0}. \tag{S57}$$

Solving for $\mathcal{E}^*$ through the equation $h_b = 0$, and then series expanding the expression $(a_1 - f\hbar c_s)^2 - 4a_2a_0$ in powers of small $\mathcal{E} - \mathcal{E}^*$, we find that $(a_1 - f\hbar c_s)^2 - 4a_2a_0 \sim \mathcal{E}^* - \mathcal{E}$, so $h_b \sim \sqrt{\mathcal{E}^* - \mathcal{E}}$.

2. *Estimate of w_b*

To estimate w_b (see Fig. S7(a)), we define a circular coordinate system shown in Fig. S7(b) whose origin is

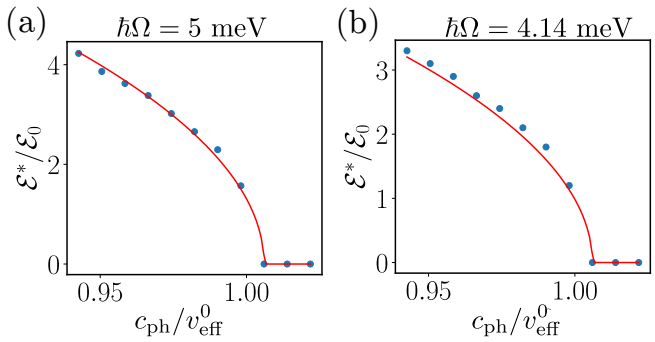

FIG. S8. Comparing numerical evaluation of $\mathcal{E}^*$ (points) to an analytic fit to Eq. S65. We use the same fitting parameters $f_2 = 0.778$, $f_1 = 0$, and $\delta(N) = 0.006$ for both panels.

the K point and arc length w is zero along the KR slice, increasing counterclockwise. The quasienergy $\varepsilon(w)$ along the circle perimeter varies with w; let us approximate

$$\varepsilon(w) \approx \hbar\Omega/2 - (d_0 + d_2 w^2), \tag{S58}$$

using some fitting parameters d_0 and d_2. (We assume that $w = 0$ is at local maximum of $\epsilon(w)$, so there is no linear term in Eq. S58.) Roughly, $w_b = w_+ - w_-$, where we find w_+ and w_- by finding the roots of the equation

$$\hbar\Omega/2 - \Delta(w) = f\hbar c_s q_m. \tag{S59}$$

Here, once again, we use the factor f in Eq. S55 to account for band flattening as $\mathcal{E}$ increases from zero. So,

$$w_b = w_+ - w_- = 2\sqrt{(f\hbar c_s q_m + \hbar\Omega/2 - d_0)/d_2}. \tag{S60}$$

Solving for $\mathcal{E}^*$ by setting $w_b = 0$ and series expanding $f\hbar c_s q_m + \hbar\Omega/2 - d_0$ in powers of $\mathcal{E}$, we find that $w_b \sim \sqrt{\mathcal{E}^* - \mathcal{E}}$.

3. *Estimate of $\mathcal{A}_{\rm in}$*

In the limit $\mathcal{E} \to \mathcal{E}^*$, the elliptical annulus with finite thickness collapses into a filled ellipse. Thus, in the limit $\mathcal{E} \to \mathcal{E}^*$, we estimate that $\mathcal{A}_{\rm in} = \pi h_b(\mathcal{E}) w_b(\mathcal{E}) \propto \max(\mathcal{E}^* - \mathcal{E}, 0)$.

VIII. PREDICTING $\mathcal{E}^*$ FOR THE TOY MODEL

Here, we use the quasienergy dispersion of the toy model to predict $\mathcal{E}^*$. By writing an approximate, analytic expression for $v_{\rm eff}(\mathcal{E})$ (see Eq. 6), we can find $\mathcal{E}^*$ using the relation $v_{\rm eff}(\mathcal{E}^*) = c_{\rm ph}$. From Eq. 6, $v_{\rm eff}(\mathcal{E}) = (\varepsilon_{\boldsymbol{k}^*+} - \varepsilon_{\boldsymbol{K}+})/|\boldsymbol{k}^* - \boldsymbol{K}|$ for some appropriately-chosen $\boldsymbol{k}^*$ (dropping the superlattice valley index for notational simplicity). One can find numerically that $\boldsymbol{k}^*$ does not shift significantly with Ω or $\mathcal{E}$. We write an ansatz

$$\varepsilon_{\boldsymbol{k}^*+} \approx \hbar v^0_{\rm eff}|\boldsymbol{k}^* - \boldsymbol{K}| - \frac{\hbar v_F}{L_M}\left(f_1'\tilde{\mathcal{E}} + f_2'\tilde{\mathcal{E}}^2\right)\frac{|\boldsymbol{k}^* - \boldsymbol{K}|}{\Omega/(2v^0_{\rm eff})}, \tag{S61}$$

where f_1' and f_2' are fitting constants dependent on the quasienergy bandstructure. Here, $\hbar v_F/L_M$ is the order of magnitude energy scale of the resonance ring gap Δ_R. The dependence of $\varepsilon_{\boldsymbol{k}^*+}$ on $\mathcal{E}$ arises predominantly from Δ_R. The dependence is stronger when $\boldsymbol{k}^*$ is close to the resonance ring, and we encode this behavior in the ratio $|\boldsymbol{k}^* - \boldsymbol{K}|/\Omega/(2v^0_{\rm eff})$, where $\Omega/(2v^0_{\rm eff})$ is the $\boldsymbol{k}$-space distance between the K point and the resonance ring. Separately, we know that $\varepsilon_{\boldsymbol{K}+} = \Delta_K/2$. We use Eq. 6 to infer

$$v^0_{\rm eff}(\mathcal{E}) = v^0_{\rm eff} - \frac{\Delta_K}{2\hbar|\boldsymbol{k}^* - \boldsymbol{K}|} - \frac{2\hbar v_F v^0_{\rm eff}}{L_M\Omega}\left(f_1'\tilde{\mathcal{E}} + f_2'\tilde{\mathcal{E}}^2\right). \tag{S62}$$

We know that $v^0_{\rm eff} \propto v_F$. We also assume that $|\boldsymbol{k}^* - \boldsymbol{K}|$ does not change significantly with $\mathcal{E}$, so it is independent of the drive and only dependent on the superlattice scale: $|\boldsymbol{k}^* - \boldsymbol{K}| \propto L_M^{-1}$. Thus, we can absorb some unknown coefficients into new coefficients f_1'' and f_2'' to obtain

$$v^0_{\rm eff}(\mathcal{E}) = v^0_{\rm eff} - \frac{\hbar v_F^2}{L_M\Omega}\left(f_1''\tilde{\mathcal{E}} + f_2''\tilde{\mathcal{E}}^2\right). \tag{S63}$$

Upon solving for $\tilde{\mathcal{E}}^*$ from $c_s = v_{\rm eff}(\mathcal{E}^*)$, we find that

$$\tilde{\mathcal{E}}^* \approx \sqrt{\frac{L_M\Omega}{3f_2 v_F}}\left(\sqrt{1 - c_{\rm ph}/v^0_{\rm eff} + f_1^2} - f_1\right), \tag{S64}$$

where f_1 and f_2 are new, rescaled fitting constants. Using the relation $\tilde{\mathcal{E}} = eL_M\mathcal{E}/(\sqrt{3}\hbar\Omega)$, we find

$$\mathcal{E}^* \approx \frac{\hbar\Omega^{3/2}}{f_2 e L_M^{1/2} v_F^{1/2}}\left(\sqrt{1 - c_{\rm ph}/v^0_{\rm eff} + f_1^2} - f_1\right), \tag{S65}$$

As $c_{\rm ph} \to v^0_{\rm eff}$, $\mathcal{E}^* \propto (1 - c_{\rm ph}/v^0_{\rm eff})^\gamma$ where $\gamma = 1$ $(1/2)$ if $f_1 \neq 0$ $(= 0)$. See Fig. S8 for a fit for two different frequencies Ω.

Finite grid size effects on an $N \times N$ Monkhorst-Pack grid (see Sec. XV) generate a small numerical error $\delta(N)$ that enters S65 as

$$\mathcal{E}^* \approx \frac{\hbar L_M^{1/2}\Omega^{3/2}}{f_2 e L_M v_F^{1/2}}\left(\sqrt{1 - c_{\rm ph}/v^0_{\rm eff} + \delta(N) + f_1^2} - f_1\right). \tag{S66}$$

To see this, let us consider the details of the finite-sized grid. We impose energy conservation through a broadened Dirac Delta function (see Sec. XV A), which we model as a Gaussian function in energy with a tiny width

$$\sqrt{2}\sigma \approx 0.1 \cdot \sqrt{2} \cdot \frac{W}{2N/3}. \tag{S67}$$

(We motivate the choice of the prefactor of 0.1 in Sec. XV A.) Since we avoid the high symmetry K point in

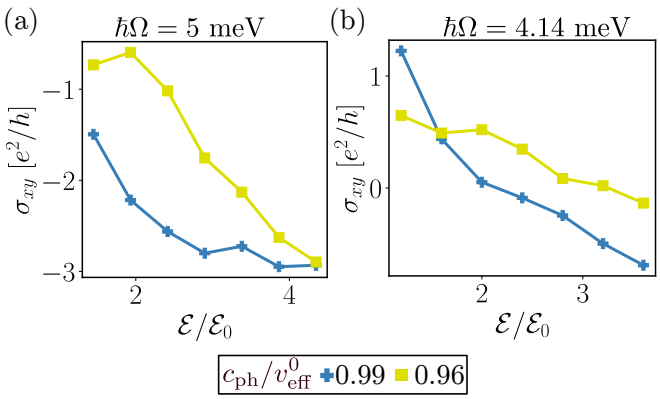

FIG. S9. Comparing the dependence of σ_{xy} on $\mathcal{E}$ for (a) the frequency considered in the main text and (b) a lower frequency where Floquet-Umklapp processes are stronger. Note that the frequency in panel (b) is inaccessible without generating two-photon resonances in the continuum model due to the peaked shape of the $\nu = \pm 1$ bands near the Γ point.

our grids, the $\boldsymbol{k}$-point with largest Berry curvature is, in fact, a point $\boldsymbol{k}_{\rm near}$ point shifted away from K by a small distance in momentum space of

$$|\delta \boldsymbol{k}| = |\boldsymbol{k}_{\rm near} - \boldsymbol{K}| \approx \frac{1}{2}\frac{\Omega/(2\hbar v^0_{\rm eff})}{2N/3} = \frac{\Omega}{4v^0_{\rm eff}(2N/3)}. \quad \text{(S68)}$$

This point is shifted in quasienergy by $\hbar v_F|\delta \boldsymbol{k}|$ relative to the actual K point. We can account for both of these effects by shifting $\varepsilon_{\boldsymbol{K}+} \to \varepsilon_{\boldsymbol{K}+} + \delta\varepsilon$, with $\delta\varepsilon = \sqrt{2}\sigma + \hbar v_F|\delta \boldsymbol{k}|$ and solve $v_{\rm eff}(\mathcal{E}^*) = c_{\rm ph}$ to find Eq. S66 with $\delta(N) = \delta\varepsilon/(\hbar v^0_{\rm eff}|\boldsymbol{k}^* - \boldsymbol{K}|)$.

IX. DIFFERENT FREQUENCIES

Reducing Ω below the value considered above will increase the ratio $(v_F e\mathcal{E}/\Omega^2)^2$ and in turn strengthen Floquet Umklapp processes, modifying the shape of the σ_{xy} curve. We demonstrate this in Fig. S9(b) for an angular frequency $\Omega = 4.135$ meV$/\hbar$. However, such a low-frequency regime is inaccessible in the continuum model (without generating two-photon resonances) due to the peaked shape of the continuum model $\nu = \pm 1$ band near the Γ point, so we do not consider this lower (doubly-resonant) frequency regime in the main text.

X. GAP SIZES

In this section, we estimate the size of the Floquet-induced gaps Δ_K and Δ_R. By the rotating wave approximation, the Floquet-induced gap at the resonance ring, Δ_R, is roughly proportional to the drive energy [10]. For a resonant drive that couples electronic states near the

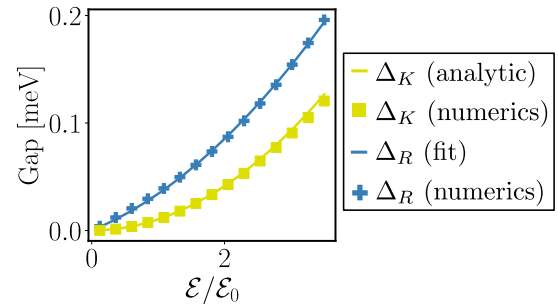

FIG. S10. Comparison of the fitted Δ_R and predicted Δ_K in Equations S72 and S76 (solid lines) to those obtained from numerics (points), using $\hbar\Omega = 5$ meV in the toy model. Here, we fit Δ_R with factors of $f_1^R = 0.04$ and $f_2^R = 0.0184$ (see Eq. S72).

Dirac points, the drive energy is roughly

$$v_F eA/\hbar, \quad \text{(S69)}$$

as predicted by minimal coupling $\boldsymbol{q} \to \boldsymbol{q} + e\boldsymbol{A}(t)/\hbar$ in the Dirac cone Hamiltonian

$$H_K(\boldsymbol{q}) = \hbar v_F \boldsymbol{q} \cdot (\xi\sigma_x, \sigma_y) \quad \text{(S70)}$$

with $v_F = WL_M/(2\sqrt{3}\hbar)$. (We always use perturbative drives that generally fall in the range of $\tilde{\mathcal{E}} < 1$.) We expect that

$$\Delta_R \approx \frac{\hbar v_F}{L_M}\tilde{\mathcal{E}}. \quad \text{(S71)}$$

Such an approximation works well for low-frequency resonant drives that couple states near the Dirac points. However, resonant drives with higher frequencies, like those used in the main text, couple states closer to the Γ-points of the TBG energy dispersion where the bands are nonlinear in q. In such a case, higher order (e.g., $\mathrm{O}(\tilde{\mathcal{E}}^2)$) contributions (from $O(q^2)$ contributions of the band-structure) to Δ_R become dominant. In the present example, the energy of the tight binding model for graphene is quadratic in momentum near the Γ point, so we write an ansatz

$$\Delta_R \approx \frac{\hbar v_F}{L_M}(f_1^R\tilde{\mathcal{E}} + f_2^R\tilde{\mathcal{E}}^2), \quad \text{(S72)}$$

and fit f_1^R and f_2^R to match Δ_R obtained by numerically diagonalizing the Floquet Hamiltonian, as shown in Fig. S10.

We can estimate the Floquet-induced K-point gap, Δ_K, by considering the time-dependent Dirac Hamiltonian

$$\begin{aligned} H_K(\boldsymbol{q}, t) = \hbar v_F(\xi q_x\sigma^x + q_y\sigma^y) \\ + v_F eA[\xi\cos(\Omega t)\sigma^x - \sin(\Omega t)\sigma^y]. \end{aligned} \quad \text{(S73)}$$

and performing a Van Vleck expansion [10–12] to obtain an effective Floquet Hamiltonian

$$H_{K,\text{eff}}(\boldsymbol{q}) = H_K^{(0)} + \frac{[H_K^{(-1)}, H_K^{(1)}]}{\hbar\Omega} = H_K + \xi \frac{e^2 v_F^2 A^2}{\hbar\Omega}\sigma^z \tag{S74}$$

with

$$H_K^{(n)}(\boldsymbol{q}) = \frac{1}{2\pi/\Omega}\int_0^{2\pi/\Omega} H_K(\boldsymbol{q},t)e^{-in\Omega t}dt. \tag{S75}$$

From Eq. S74, we can extract

$$\Delta_K = \frac{2e^2 v_F^2}{\hbar\Omega}A^2 = \frac{6\hbar v_F^2}{L_M^2\Omega}\tilde{\mathcal{E}}^2. \tag{S76}$$

XI. FLOQUET BOLTZMANN EQUATION

Here, we present the full expression for the Floquet-Boltzmann equation [13], $\partial_t F_{\boldsymbol{k}\alpha}(t) = I^{\text{el-ph}}_{\boldsymbol{k}\alpha}[\{F_{\boldsymbol{k}\alpha}(t)\}] + I^{\text{el-el}}_{\boldsymbol{k}\alpha}[\{F_{\boldsymbol{k}\alpha}(t)\}]$. The electron-phonon collision integral is

$$\begin{aligned} I^{\text{el-ph}}_{\boldsymbol{k}\alpha}[\{F_{\boldsymbol{k}\alpha}\}] = \frac{2\pi}{\hbar}\frac{1}{N}\sum_{\boldsymbol{k}'\in\text{BZ}}\sum_{\alpha'}\sum_j\sum_n |\mathcal{G}^{\boldsymbol{k}'\alpha'}_{\boldsymbol{k}\alpha}(n,j)|^2 \\ \times\Big[\big\{F_{\boldsymbol{k}'\alpha'}(1-F_{\boldsymbol{k}\alpha})\mathcal{N}(\hbar\omega_j(\boldsymbol{k}'-\boldsymbol{k})) - F_{\boldsymbol{k}\alpha}(1-F_{\boldsymbol{k}'\alpha'})[1+\mathcal{N}(\hbar\omega_j(\boldsymbol{k}'-\boldsymbol{k}))]\big\} \\ \times\delta(\varepsilon_{\boldsymbol{k}'\alpha'} - \varepsilon_{\boldsymbol{k}\alpha} + \hbar\omega_j(\boldsymbol{q}) + n\hbar\Omega) \\ + \big\{F_{\boldsymbol{k}'\alpha'}(1-F_{\boldsymbol{k}\alpha})[1+\mathcal{N}(\hbar\omega_j(\boldsymbol{k}'-\boldsymbol{k}))] - F_{\boldsymbol{k}\alpha}(1-F_{\boldsymbol{k}'\alpha'})\mathcal{N}(\hbar\omega_j(\boldsymbol{k}'-\boldsymbol{k}))\big\} \\ \times\delta(\varepsilon_{\boldsymbol{k}'\alpha'} - \varepsilon_{\boldsymbol{k}\alpha} - \hbar\omega_j(\boldsymbol{q}) + n\hbar\Omega)\Big] \end{aligned} \tag{S77}$$

$$\mathcal{G}^{\boldsymbol{k}'\alpha'}_{\boldsymbol{k}\alpha}(n,j) = \frac{1}{\sqrt{A_{\text{Moiré}}}}\frac{D}{\sqrt{2\rho}c_{\text{ph}}}\sqrt{\hbar\omega_j(\boldsymbol{k}'-\boldsymbol{k})}\sum_m\sum_{\nu,\nu'}\langle\phi^{n+m}_{\boldsymbol{k}'\alpha'}|\nu'\boldsymbol{k}'\rangle\mathcal{W}^{\xi\nu'\nu}_{\boldsymbol{k},\boldsymbol{k}+\boldsymbol{G}_j}\langle\nu\boldsymbol{k}|\phi^m_{\boldsymbol{k}\alpha}\rangle \tag{S78}$$

where $\rho = 7.61\times10^{-7}$ kg/m^2 is the 2D density of the graphene layers, D is the deformation potential, and the acoustic phonon mode j has frequency $\omega_j(\boldsymbol{q}) = \hbar c_{\text{ph}}|\boldsymbol{q}+\boldsymbol{G}_j|$ with $\{\boldsymbol{G}_j\}$ being the set of all possible reciprocal lattice vectors. The function $\mathcal{N}(\varepsilon) = (e^{-\varepsilon/k_B T_{\text{ph}}} - 1)^{-1}$ is the Bose-Einstein occupation of the phonon bath at temperature T_{ph}. The electron-electron collision integral is

$$\begin{aligned} I^{\text{el-el}}_{\boldsymbol{k}\alpha}[\{F_{\boldsymbol{k}\alpha}\}] = \frac{4\pi}{\hbar}\frac{1}{N^2}\sum_{\boldsymbol{k}_2\in\text{BZ}}\sum_{\boldsymbol{k}_3\in\text{BZ}}\sum_{\alpha_2,\alpha_3,\alpha_4}\sum_n\sum_{\boldsymbol{G}}|\mathcal{V}^{(\boldsymbol{k}_3,\alpha_3),(\boldsymbol{k}_1+\boldsymbol{k}_2-\boldsymbol{k}_3,\alpha_4)}_{(\boldsymbol{k},\alpha),(\boldsymbol{k}_2,\alpha_2)}(n,\boldsymbol{G})|^2\times \\ \times\delta(\varepsilon_{\boldsymbol{k}\alpha} + \varepsilon_{\boldsymbol{k}_2\alpha_2} - \varepsilon_{\boldsymbol{k}_3\alpha_3} - \varepsilon_{\boldsymbol{k}+\boldsymbol{k}_2-\boldsymbol{k}_3,\alpha_4} + n\hbar\Omega)\times \\ \times[(1-F_{\boldsymbol{k}\alpha})(1-F_{\boldsymbol{k}_2\alpha_2})F_{\boldsymbol{k}_3\alpha_3}F_{\boldsymbol{k}_1+\boldsymbol{k}_2-\boldsymbol{k}_3,\alpha_4} - F_{\boldsymbol{k}\alpha}F_{\boldsymbol{k}_2\alpha_2}(1-F_{\boldsymbol{k}_3\alpha_3})(1-F_{\boldsymbol{k}_1+\boldsymbol{k}_2-\boldsymbol{k}_3,\alpha_4})] \end{aligned} \tag{S79}$$

$$\begin{aligned} \mathcal{V}^{(\boldsymbol{k}_3,\alpha_3),(\boldsymbol{k}_1+\boldsymbol{k}_2-\boldsymbol{k}_3,\alpha_4)}_{(\boldsymbol{k},\alpha),(\boldsymbol{k}_2,\alpha_2)}(n) = \sum_{\nu_1,\nu_2}\sum_{\nu_3,\nu_4}\sum_{n_2,n_3,n_4} V_{\boldsymbol{k}_2-\boldsymbol{k}_3+\boldsymbol{G}}\mathcal{W}^{\xi\nu_1\nu_4}_{\boldsymbol{k}_1,\boldsymbol{q}+\boldsymbol{G}}\mathcal{W}^{\xi\nu_2\nu_3}_{\boldsymbol{k}_2,-\boldsymbol{q}-\boldsymbol{G}}\langle\phi^{n-n_2+n_3+n_4}_{\boldsymbol{k}\alpha}|\nu_1\boldsymbol{k}\rangle\langle\phi^{n_2}_{\boldsymbol{k}_2\alpha_2}|\nu_2\boldsymbol{k}_2\rangle\times \\ \times\langle\nu_3\boldsymbol{k}_3|\phi^{n_3}_{\boldsymbol{k}_3\alpha_3}\rangle\langle\nu_4\boldsymbol{k}_4|\phi^{n_4}_{\boldsymbol{k}+\boldsymbol{k}_2-\boldsymbol{k}_3,\alpha_4}\rangle. \end{aligned} \tag{S80}$$

We solve for $\partial_t F_{\boldsymbol{k}\alpha} = 0$ using the Newton-Raphson algorithm. To ensure charge neutrality, we add a Lagrange multiplier term $\lambda(\sum_{\boldsymbol{k}\alpha}F_{\boldsymbol{k}\alpha} - N)$ to the Floquet-Boltzmann equation, choosing some large constant λ.

XII. FORM FACTOR DETAILS

Here, we discuss the details of the form factors $\mathcal{W}^{\xi\nu'\nu}_{\boldsymbol{k},\boldsymbol{q}+\boldsymbol{G}}$ used in the Boltzmann equation. In the continuum model, we calculate the form factor directly from the wavefunctions:

$$\mathcal{W}^{\xi\nu'\nu}_{\boldsymbol{k},\boldsymbol{q}+\boldsymbol{G}} = \sum_{X,\boldsymbol{G}'} C^{X*}_{\nu'\boldsymbol{k}+\boldsymbol{q}}(\boldsymbol{G}'-\boldsymbol{G})C^{X}_{\nu\boldsymbol{k}}(\boldsymbol{G}'). \tag{S81}$$

For the toy model, we include, by hand, a suppression factor $e^{-l_w^2|\boldsymbol{q}+\boldsymbol{G}|^2/4}$, which accounts for the moiré periodicity that the toy model is unable to capture [14]:

$$\mathcal{W}^{\xi\nu'\nu}_{\boldsymbol{k},\boldsymbol{q}+\boldsymbol{G}} = \langle \xi\nu'\boldsymbol{k}+\boldsymbol{q}|\xi\nu\boldsymbol{k}\rangle e^{-l_w^2|\boldsymbol{q}+\boldsymbol{G}|^2/4}. \tag{S82}$$

We choose $l_w = L_M/(1.5\sqrt{3})$ so that the form factor dependence on $|\boldsymbol{q}+\boldsymbol{G}|$ captures that of the continuum model.

To check the agreement between the toy and continuum model form factors, we calculate the form factors on a $\boldsymbol{k}$-grid, with a set of reciprocal lattice vectors $\{\boldsymbol{G}\}$, and plot the average value of $\mathcal{W}^{\xi\nu'\nu}_{\boldsymbol{k},\boldsymbol{q}+\boldsymbol{G}}$ as a function of $|\boldsymbol{q}+\boldsymbol{G}|$, for $\boldsymbol{k}$ at the K, Γ, and M points of the mini Brillouin zone. The results, shown in Fig. S11, show that the toy model form factor captures the general features of that of the continuum model.

We can show analytically that the toy and continuum model form factors agree when $\boldsymbol{k}$ and $\boldsymbol{k}+\boldsymbol{q}$ lie within the same K or K' valley in the mini Brillouin zone. These low-momentum transfer processes are crucial to the tunable σ_{xy} presented in the text. Let us write $\boldsymbol{k} \equiv \boldsymbol{K}+\boldsymbol{p}$ (and $\boldsymbol{k}+\boldsymbol{q} = \boldsymbol{K}+\boldsymbol{p}+\boldsymbol{q}$), where $|\boldsymbol{q}|$ and $|\boldsymbol{p}|$ are small enough such that the energy dispersion still resembles a Dirac cone at momenta $\boldsymbol{k}$ and $\boldsymbol{k}+\boldsymbol{q}$. By utilizing the eigenfunctions of the Dirac cone Hamiltonian, one can show that the form factors are

$$\mathcal{W}^{\xi\nu'\nu}_{\boldsymbol{K}+\boldsymbol{p},\boldsymbol{q}} = \frac{1}{2}\left(1+\nu\nu'\frac{\boldsymbol{p}\cdot(\boldsymbol{p}+\boldsymbol{q})}{|\boldsymbol{p}||\boldsymbol{p}+\boldsymbol{q}|}\right). \tag{S83}$$

The formula holds true regardless of the chirality of the Dirac nodes. Note that form factors representing direct (non-FU) scattering transitions between different K and K' valleys in the mini Brillouin zone are not relevant since such scattering transitions are kinematically prohibited due to the slow-electron regime.

XIII. VALIDITY OF THE DIAGONAL DENSITY MATRIX APPROXIMATION

In general, one needs to keep track of all coherences between the Floquet states, $\langle \hat{f}^{(\xi)\dagger}_{\boldsymbol{k}\alpha}(t)\hat{f}^{(\xi)}_{\boldsymbol{k}'\alpha'}(t)\rangle$, to fully-characterize the steady-state of a Floquet system. Translation symmetry suppresses the coherences for $\boldsymbol{k}\neq\boldsymbol{k}'$. The $\alpha\neq\alpha'$ interband coherences are suppressed for $\tau^{\text{tot}}_{\boldsymbol{k}} \gg \hbar/\Delta\varepsilon_{\boldsymbol{k}}$, where $1/\tau^{\text{tot}}_{\boldsymbol{k}} = 1/\tau^{\text{el}}_{\boldsymbol{k}} + 1/\tau^{\text{ph}}_{\boldsymbol{k}}$, $1/\tau^{\text{el}}_{\boldsymbol{k}}$ and $1/\tau^{\text{ph}}_{\boldsymbol{k}}$ are the interband electron-electron and electron-phonon scattering rates, respectively, and $\Delta\varepsilon_{\boldsymbol{k}} = \min_{n\in\mathbb{Z}}|\varepsilon_{\boldsymbol{k}+} - \varepsilon_{\boldsymbol{k}-} + n\hbar\Omega|$. In this section, we will explain how we numerically estimate the scattering rates.

A. Formal Definition of Scattering Times

Following Ref. [15], we define the interband scattering rates (fixing the initial Floquet band α) as

$$\begin{aligned}\frac{1}{\tau^{\text{ph}}_{\boldsymbol{k}}} = \frac{2\pi}{\hbar}\frac{1}{N}\sum_{\boldsymbol{k}'\in\text{BZ}}\sum_{\alpha'\neq\alpha}\sum_{j}\sum_{n}|\mathcal{G}^{\boldsymbol{k}'\alpha'}_{\boldsymbol{k}\alpha}(n,j)|^2\Big[&(1-F_{\boldsymbol{k}'\alpha'})[1+\mathcal{N}(\hbar\omega_j(\boldsymbol{k}'-\boldsymbol{k}))]\delta(\varepsilon_{\boldsymbol{k}'\alpha'}-\varepsilon_{\boldsymbol{k}\alpha}+\hbar\omega_j(\boldsymbol{q})+n\hbar\Omega)\\ &+(1-F_{\boldsymbol{k}'\alpha'})\mathcal{N}(\hbar\omega_j(\boldsymbol{k}'-\boldsymbol{k}))\delta(\varepsilon_{\boldsymbol{k}'\alpha'}-\varepsilon_{\boldsymbol{k}\alpha}-\hbar\omega_j(\boldsymbol{q})+n\hbar\Omega)\Big],\end{aligned} \tag{S84}$$

$$\begin{aligned}\frac{1}{\tau^{\text{el}}_{\boldsymbol{k}}} = \frac{4\pi}{\hbar}\frac{1}{N^2}\sum_{\boldsymbol{k}_2\in\text{BZ}}\sum_{\boldsymbol{k}_3\in\text{BZ}}\sum_{\substack{\alpha_2,\alpha_3,\alpha_4\\ \alpha_3 \text{ or } \alpha_4\neq\alpha}}\sum_{n}\sum_{\boldsymbol{G}}|\mathcal{V}^{(\boldsymbol{k}_3,\alpha_3),(\boldsymbol{k}_1+\boldsymbol{k}_2-\boldsymbol{k}_3,\alpha_4)}_{(\boldsymbol{k},\alpha),(\boldsymbol{k}_2,\alpha_2)}(n,\boldsymbol{G})|^2\times\\ \times\delta(\varepsilon_{\boldsymbol{k}\alpha}+\varepsilon_{\boldsymbol{k}_2\alpha_2}-\varepsilon_{\boldsymbol{k}_3\alpha_3}-\varepsilon_{\boldsymbol{k}+\boldsymbol{k}_2-\boldsymbol{k}_3,\alpha_4}+n\hbar\Omega)F_{\boldsymbol{k}_2\alpha_2}(1-F_{\boldsymbol{k}_3\alpha_3})(1-F_{\boldsymbol{k}_1+\boldsymbol{k}_2-\boldsymbol{k}_3,\alpha_4}).\end{aligned} \tag{S85}$$

B. Numerical Calculation of Scattering Rates

In Fig. S12, we show the ratio $\hbar/(\tau^{\text{tot}}_{\boldsymbol{k}}\Delta\varepsilon_{\boldsymbol{k}})$ in the regimes $\mathcal{E}/\mathcal{E}_0 = 0.966 < \mathcal{E}^*/\mathcal{E}_0$ and $\mathcal{E}/\mathcal{E}_0 = 2.898 > \mathcal{E}^*/\mathcal{E}_0$ for the case $\chi = \tau^{\text{el}}_K/\tau^{\text{ph}}_K \approx 2.8$ and $\zeta = \hbar/(2\tau^{\text{tot}}_K\Delta_K) \approx 0.5$, where ζ is the maximum value across the range of $\mathcal{E}$ considered in Fig. 1(b) in the main text, and χ is evaluated at the drive amplitude at which ζ is fixed. One sees that $\hbar/(\tau^{\text{tot}}_{\boldsymbol{k}}\Delta\varepsilon_{\boldsymbol{k}}) \ll 1$ for most of the Brillouin zone and $\hbar/(\tau^{\text{tot}}_{\boldsymbol{k}}\Delta\varepsilon_{\boldsymbol{k}}) < 1$ where the interband

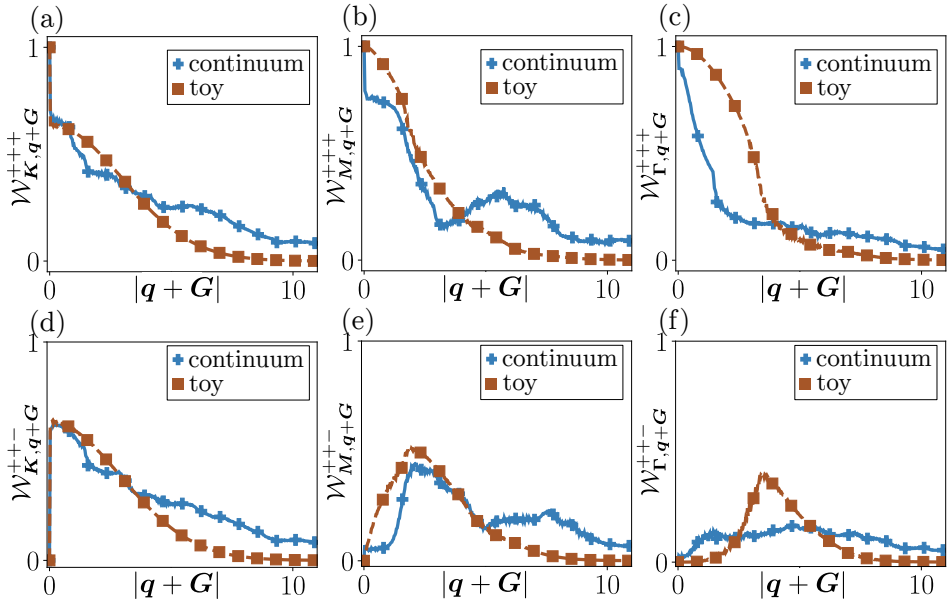

FIG. S11. Comparing the average toy and continuum model form factors $\mathcal{W}^{\xi\nu'\nu}_{\boldsymbol{k},\boldsymbol{q}+\boldsymbol{G}}$, with $|\boldsymbol{q}+\boldsymbol{G}|$ measured in units of 10^8 m^{-1}. (a-c) The intraband ($\nu = \nu'$) form factors at the K, M, and Γ points. (d-f) The interband ($\nu \neq \nu'$) form factors at the K, M, and Γ points.

gaps are the smallest; by analysis of the Floquet-Redfield equation in Refs. [15, 16], the diagonal density matrix was shown to be a good approximation in this regime. Note that the definitions in Eqs. S84 and S85 calculate the electron (rather than hole) scattering times, and hence Pauli blocking results in different scattering times for the upper and lower Floquet bands; the scattering rates quoted in the main text take the maximum rate. Separately, we also note that the toy model underestimates the resonance gap (see Fig. S1) relative to the continuum model, and therefore overestimates $\hbar/(\tau^{\text{tot}}_{\boldsymbol{k}}\Delta\varepsilon_{\boldsymbol{k}})$ around the resonance ring.

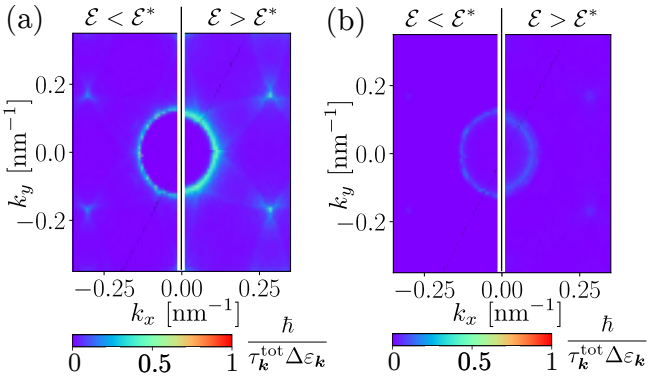

FIG. S12. The color represents the ratio $\hbar/(\tau^{\text{tot}}_{\boldsymbol{k}}\Delta\varepsilon_{\boldsymbol{k}})$ at different points in momentum space (a) for the upper Floquet band and (b) for the lower Floquet band for the case $\chi \approx 2.8$ and $\zeta \approx 0.5$.

XIV. DIELECTRIC FUNCTION OF STRONTIUM TITANATE

The dielectric function for $SrTiO_3$ is

$$\epsilon(\Omega) = \epsilon_\infty \prod_{j=1}^{3} \frac{\omega_{Lj}^2 - \Omega^2}{\omega_{Tj}^2 - \Omega^2} \tag{S86}$$

at angular frequency Ω, with the experimentally-determined longitudinal and transverse optical phonon frequencies, ω_{Lj} and ω_{Tj}, respectively, given in Ref. [17–19]. One finds that $|\epsilon(5\text{ meV})| = 1682$.

XV. MONKHORST-PACK GRID, NUMERICAL INTEGRATION, AND CONVERGENCE

In this section, we describe the methods we use to discretize the momentum Brillouin zone. We perform the Boltzmann equation integrals, introduced in Equations S77 and S79, over an $N \times N$ Monkhorst-Pack (MP) set of grid points [20], with $\boldsymbol{k}$-points

$$\boldsymbol{k}_{m,n} = \frac{m\boldsymbol{G}_1 + n\boldsymbol{G}_2}{N}, \tag{S87}$$

odd N, and $m, n = 0, \ldots, N-1$. Specifically, we avoid values of $N (\text{mod } 3) = 0$ that generate a $\boldsymbol{k}$-point exactly at the high-symmetry point of K, because such grids converge poorly when the drive strength is weak and Floquet-induced gap Δ_K is small.

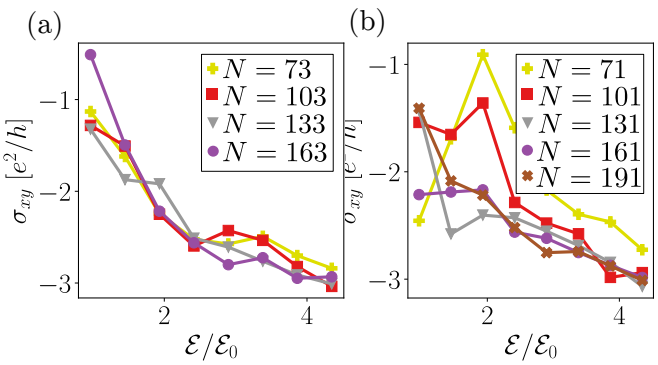

FIG. S13. Convergence of anomalous conductivity with grid size for (a) $N(\text{mod } 3) = 1$ and (b) $N(\text{mod } 3) = 2$. Due to the positioning of grid points near the K point, the results at low grid resolutions show significant disagreement.

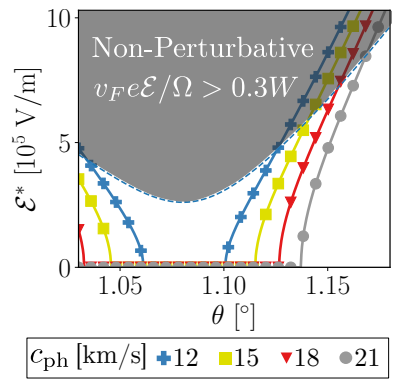

FIG. S14. The requirement that the laser drive strength $\mathcal{E}$ is perturbative, i.e. a fraction of electron bandwidth $e\mathcal{E}L_M < W$, narrows the range of $\mathcal{E}$ values that can be used. As a result, the range of c_{ph} whose $\mathcal{E}^*$ is visible is limited as well - we postulate that they are pushed to higher drive strengths $\mathcal{E}$.

A. Energy and Momentum Conservation

Here, we discuss in detail how we impose momentum and energy conservation on this MP grid. The space of MP $\boldsymbol{k}$ vectors are closed under addition and subtraction (modulo a reciprocal lattice vector), so conservation of momentum (e.g., $\boldsymbol{k}+\boldsymbol{k}_2-\boldsymbol{k}_3$ in Eq. S79), is simple to implement. We impose energy conservation via a smeared Dirac Delta function

$$\delta(\varepsilon) = \begin{cases} 1.04766 e^{-\varepsilon^2/2\sigma^2}/(2.5066283\sigma), & \text{if } |\varepsilon| < 2\sigma, \\ 0, & \text{otherwise,} \end{cases} \tag{S88}$$

where we have chosen numerical factors so that

$$\int_{-\infty}^{\infty} \delta(\varepsilon) d\varepsilon = 1. \tag{S89}$$

The smearing parameter σ is one-tenth of the maximum quasienergy spacing between nearest-neighbor MP $\boldsymbol{k}$-points

$$\sigma = 0.1 \max_{\langle \boldsymbol{k},\boldsymbol{k}'\rangle,\alpha} |\varepsilon^{(\xi)}_{\boldsymbol{k}\alpha} - \varepsilon^{(\xi)}_{\boldsymbol{k}'\alpha}|, \tag{S90}$$

where $\langle \boldsymbol{k},\boldsymbol{k}'\rangle$ restricts $\boldsymbol{k}'$ to be a nearest-neighbor of $\boldsymbol{k}$, and we have tuned the prefactor of 0.1 so that upon calculating the steady-state without Floquet-Umklapp processes, we obtain a Fermi-Dirac distribution, $F^{(\xi)}_{\boldsymbol{k}\alpha} = (e^{\varepsilon_{\boldsymbol{k}\alpha}/k_B T_{\text{ph}}} + 1)^{-1}$ with temperature T_{ph} of the phonon bath [21].

B. Convergence of Conductivities

In Fig. S13, we show the convergence of the Hall conductivity σ_{xy} with grid size, using $\hbar\Omega = 5$ meV. In the main text, we use a 163×163 MP grid for non-interacting calculations, and a 73×73 grid for interacting calculations.

XVI. BERRY CURVATURE CALCULATIONS

We follow the Berry curvature calculation presented in [22], defining U(1) link variables

$$U_\mu(\boldsymbol{k},t) = \frac{\langle\alpha(\boldsymbol{k},t)|\alpha(\boldsymbol{k}+\hat{\boldsymbol{\mu}},t)\rangle}{|\langle\alpha(\boldsymbol{k},t)|\alpha(\boldsymbol{k}+\hat{\boldsymbol{\mu}},t)\rangle|} \tag{S91}$$

where $\mu = x, y$, $\hat{\boldsymbol{\mu}} = \boldsymbol{G}_\mu/N$, and $|\alpha(\boldsymbol{k},t)\rangle$ are the Bloch vectors (i.e., $|\psi_{\boldsymbol{k}\alpha}(t)\rangle = e^{-i\boldsymbol{k}\cdot\boldsymbol{r}}|\alpha(\boldsymbol{k},t)\rangle$). The Berry curvature is

$$\mathcal{B}_{\boldsymbol{k}\alpha}(t) = \frac{(2\pi)^2}{N^2 A_M} \arg\left[\frac{U_x(\boldsymbol{k},t)U_y(\boldsymbol{k}+\hat{\boldsymbol{x}},t)}{U_x(\boldsymbol{k}+\hat{\boldsymbol{y}},t)U_y(\boldsymbol{k},t)}\right] \tag{S92}$$

and we use the time-averaged Berry curvature

$$\mathcal{B}_{\boldsymbol{k}\alpha} \equiv \frac{1}{2\pi/\Omega}\int_0^{2\pi/\Omega} \mathcal{B}_{\boldsymbol{k}\alpha}(t)dt \tag{S93}$$

in transport calculations.

XVII. THE DRIVE AMPLITUDE PERTURBATIVE REGIME AT DIFFERENT TWIST ANGLES

We have treated the laser drive as a perturbation to the undriven TBG Hamiltonian, which restricts the range of field strengths $\mathcal{E}$ we can use to a weak perturbative regime. This also narrows the range of phonon speeds c_{ph} that will generate a critical field strength $\mathcal{E}^*$ in the perturbative regime, hence the narrow range of c_{ph} we have considered in, e.g., Fig. 1(c). For various twist angles, we estimate the range of drive strengths $\mathcal{E}$ that are perturbative in the unshaded region of Fig. S14 and overlap in solid lines the predicted value of $\mathcal{E}^*$ for different speeds of sound. The shaded, non-perturbative regime

corresponds to drive energy scales $v_F e\mathcal{E}/\Omega$ greater than a fraction, e.g., 0.3, of the bandwidth W. Here, we follow the analysis in [4] to estimate the undriven Fermi velocity

$$v_F(\theta) = \sqrt{\left((1-3\alpha^2)/(1+3\alpha^2(1+\eta^2)) \times v_F^{\mathrm{ml}}\right)^2 + v_{\mathrm{min}}^2}, \tag{S94}$$

where $v_{\mathrm{min}} = 10^4$ m/s is a manually set minimum Fermi velocity of the undriven flat bands, and we use the same parameters as in Sec. II. We also adjust Ω such that $\Omega/v_F(\theta)$ is constant and equal to those considered in Figs. 1-4.

[1] M. S. Rudner and N. H. Lindner, "The floquet engineer's handbook," (2020), arXiv:2003.08252 [cond-mat].

[2] Q. Chen, L. Du, and G. A. Fiete, Phys. Rev. B **97**, 035422 (2018).

[3] M. Koshino, N. F. Q. Yuan, T. Koretsune, M. Ochi, K. Kuroki, and L. Fu, Phys. Rev. X **8**, 031087 (2018).

[4] R. Bistritzer and A. Macdonald, Proceedings of the National Academy of Sciences of the United States of America **108** (2010), 10.1073/pnas.1108174108.

[5] O. Katz, G. Refael, and N. H. Lindner, Phys. Rev. B **102**, 155123 (2020).

[6] B. A. Bernevig, Z.-D. Song, N. Regnault, and B. Lian, Phys. Rev. B **103**, 205413 (2021).

[7] Z.-D. Song, B. Lian, N. Regnault, and B. A. Bernevig, Phys. Rev. B **103**, 205412 (2021).

[8] Z. Song, Z. Wang, W. Shi, G. Li, C. Fang, and B. A. Bernevig, Phys. Rev. Lett. **123**, 036401 (2019).

[9] O. Karni, I. Esin, and K. M. Dani, Advanced Materials **n/a**, 2204120.

[10] M. Rudner and N. Lindner, Nature Reviews Physics **2**, 1 (2020).

[11] M. Rodriguez-Vega, M. Vogl, and G. Fiete, Annals of Physics **435**, 168434 (2021).

[12] T. Kitagawa, T. Oka, A. Brataas, L. Fu, and E. Demler, Phys. Rev. B **84**, 235108 (2011).

[13] K. I. Seetharam, C.-E. Bardyn, N. H. Lindner, M. S. Rudner, and G. Refael, Phys. Rev. B **99**, 014307 (2019).

[14] H. Ishizuka, A. Fahimniya, F. Guinea, and L. Levitov, Nano Letters **21**, 7465 (2021), pMID: 34515488, https://doi.org/10.1021/acs.nanolett.1c00565.

[15] K. I. Seetharam, C.-E. Bardyn, N. H. Lindner, M. S. Rudner, and G. Refael, Phys. Rev. X **5**, 041050 (2015).

[16] K. I. Seetharam, *Thermalization in Periodically-Driven Interacting Quantum Systems*, Ph.D. thesis, California Institute of Technology, Pasadena (2018).

[17] J. Ruhman and P. A. Lee, Phys. Rev. B **94**, 224515 (2016).

[18] H. Vogt and G. Rossbroich, Phys. Rev. B **24**, 3086 (1981).

[19] P. Dore, A. Paolone, and R. Trippetti, Journal of Applied Physics **80**, 5270 (1996), https://doi.org/10.1063/1.363513.

[20] H. J. Monkhorst and J. D. Pack, Phys. Rev. B **13**, 5188 (1976).

[21] V. M. Galitskii and V. F. Elesin, Journal of Experimental and Theoretical Physics **30** (1970).

[22] T. Fukui, Y. Hatsugai, and H. Suzuki, Journal of the Physical Society of Japan **74**, 1674 (2005), https://doi.org/10.1143/JPSJ.74.1674